Radon transform-based microseismic event detection and signal-to-noise ratio enhancement

Juan I. Sabbione [a,*], Mauricio D. Sacchi [b], Danilo R. Velis [a]

[a] Facultad de Ciencias Astronómicas y Geofísicas, Universidad Nacional de La Plata, and CONICET, Paseo del Bosque s/n, La Plata B1900FWA, Argentina
[b] Department of Physics and Signal Analysis and Imaging Group (SAIG), University of Alberta, 4-183 CCIS, Edmonton, AB T6G 2E1, Canada

ARTICLE INFO

ABSTRACT

We present an adaptive filtering method to denoise downhole microseismic data. The methodology uses the apex-shifted parabolic Radon transform. The algorithm is implemented in two steps. In the first step we apply the apex-shifted parabolic Radon transform to the normalized root mean square envelope of the microseismic data to detect the presence of an event. The Radon coefficients are efficiently calculated by restricting the integration paths of the Radon operator. In a second stage, a new (preconditioned) Radon transform is applied to individual components to enhance the recorded signal. The denoising is posed as an inverse problem preconditioned by the Radon coefficients obtained in the previous step. The algorithm was tested with synthetic and field datasets that were recorded with a vertical array of receivers. The method performs rapidly due to the parabolic approximation making it suitable for real-time monitoring. The P– and S–wave direct arrivals are properly denoised for high to moderate signal-to-noise ratio records.

© 2014 Elsevier B.V. All rights reserved.

1. Introduction

Low permeability reservoirs require fluid injection in order to fracture the bedrock and favor hydrocarbon extraction. This gives rise to a broad set of geophysical applications designed to monitor the reservoir dynamics while controlling the injection process. The microseismicity induced by the hydraulic fracturing is characterized by small magnitude micro-earthquakes (Maxwell and Urbancic, 2001). Therefore, microseismic data are generally acquired in low signal-to-noise (S/N) environments. Furthermore, inadequate array coverage and imprecise knowledge of subsurface P– and S–wave velocity models complicate the detection and location of microseismic events (Eisner et al., 2009).

Microseismic acquisition projects can be divided according to two different scenarios: surface and downhole monitoring. This paper focuses on downhole geometries and on the problem of detecting and enhancing microseismic events. Downhole acquisition configurations involve arrays of three-component geophones buried in vertical or deviated boreholes close to the injection well (Maxwell and Rutledge, 2010).

Noise-suppression has become an important challenge to precondition microseismic data for the estimation of the event location and inversion of the seismic moment tensor. Accurate locations and moment tensor information are of paramount importance for the correct derivation of fracture positions and source mechanisms (Eisner et al., 2011; Kendall et al., 2011; Leaney, 2008; Vera Rodriguez et al., 2012). Thus, signal enhancement techniques are an important component of current efforts to properly analyze and invert microseismic data. In this sense, Vera Rodriguez et al. (2012) introduced a time-frequency basis pursuit denoising algorithm for multicomponent microseismic data. Recently, Forghani-Arani et al. (2013) proposed a $\tau - p$ transform to suppress noise in microseismic data acquired by surface arrays. In this article we focus our attention to the problem of denoising borehole microseismic data via the apex-shifted parabolic Radon transform (ASPRT) (Hargreaves et al., 2003; Trad, 2003).

In reflection seismology, Radon transforms have been widely used to increase the S/N of seismic gathers and to remove multiple reflections (Hampson, 1986; Russell et al., 1990a, 1990b; Yilmaz, 1989). In this paper, we propose to detect microseismic signal arrivals and denoise the data using an adaptive filtering method that follows a Radon transform formulation that is often utilized in reflection seismology.

This paper is organized as follows. We first describe the two-stage algorithm for microseismic data denoising. The first stage is used for the detection while the second is used for the denoising. For the detection, we use the apex-shifted parabolic Radon transform of the normalized root mean square envelope of the microseismic data, which is similar to the 3C envelope energy suggested by Michaud and Leaney (2008). Then, we use this information to determine a support region in the Radon domain that contains the signal arrivals (P– and S–waves). This permits to enhance the S/N of each component of the data by posing the Radon representation of the data as an inverse problem with restricted support. We first evaluate the algorithm with
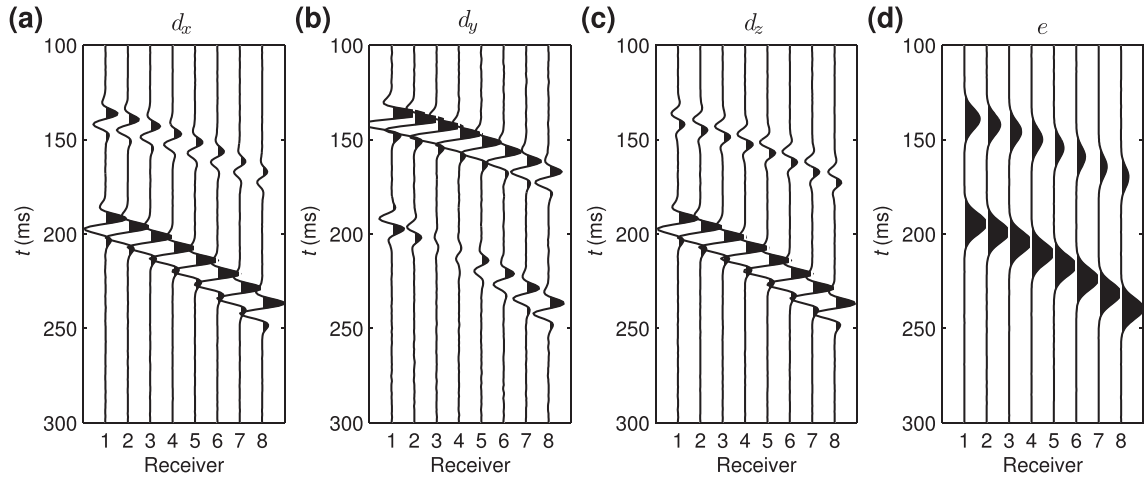
Fig. 1. Synthetic dataset 1: $S/N = 100$ (negligible noise). (a) x-component. (b) y-component. (c) z-component. (d) Normalized root mean square envelope attribute e.

synthetic datasets. Then, we evaluate it with field datasets that portray different noise levels. In addition, we include a discussion section and an appendix to analyze the validity of the parabolic approximation and the reliability of the results in view of the algorithm's parameters selection.

2. Method

We present a two-step method to detect and denoise microseismic events. For this purpose, we utilize the apex-shifted parabolic Radon transform (ASPRT) first introduced in reflection seismology to attenuate diffracted multiples (Hargreaves et al., 2003; Trad, 2003).

2.1. Parabolic approximation

We consider a constant velocity 2D medium. Let us assume an array of receivers with coordinates (x, z) deployed on a vertical borehole close to the source of microseismic events. For this geometry, the recorded travel-times for a seismic event occurring at coordinates (x_s, z_s) is given by

$$t(z) = t_0 + \sqrt{\frac{(x-x_s)^2}{v^2} + \frac{(z-z_s)^2}{v^2}}, \quad (1)$$

where t_0 is the time of the event relative to the origin of the recording time and v is the P– or S–wave velocity of the medium. We can rewrite Eq. (1) via the following expression

$$t(z) = t_0 + \sqrt{t_a^2 + \frac{(z-z_s)^2}{v^2}}, \quad (2)$$

where $t_a = (x - x_s)/v$. Eq. (2) represents an apex-shifted hyperbola with the apex shifted by z_s and the time of the apex relative to the origin of the recording time given by $t_0 + t_a$.

We can now introduce the following parabolic approximation

$$
\begin{aligned}
t(z) &= t_0 + t_a \sqrt{1 + \frac{(z-z_s)^2}{t_a^2 v^2}} \\
&\approx t_0 + t_a + q(z-z_s)^2 \\
&\approx \tau + q(z-z_s)^2,
\end{aligned}
\quad (3)
$$

where t_0 and t_a were combined into a single time variable $\tau = t_0 + t_a$ and the curvature of the parabola is given by

$$q = \frac{1}{2 t_a v^2}. \quad (4)$$

Thus, we obtain the expression of the shifted parabola that we will utilize for our Radon transform. It is worth mentioning that the parameter q in Eq. (4) is interpreted as an effective curvature that in real scenarios might not yield a realistic velocity v (Blias and Grechka, 2013; Yilmaz, 2001). In other words, we will not use the estimated parameter q to infer velocity information via Eq. (4). In fact, q is interpreted as a kinematic parameter to stack energy across parabolic paths.

By adopting the parabolic approximation we have replaced the two temporal variables t_0 and t_a by a single variable τ. The integration path given by Eq. (3) leads to the so called ASPRT (Hargreaves et al., 2003; Trad, 2003). The validity of the parabolic approximation for constant velocity media is discussed in Appendix A.

2.2. Event detection via the ASPRT

We denote the three-component data recorded by a vertical array of receivers by $d_x(t,z_j), d_y(t,z_j)$ and $d_z(t,z_j)$, $j = 1 \ldots N$, where z_j is the vertical position for the receiver j and N is the number of receivers of the array. We also define the envelope of the x, y and z components by $e_x(t, z_j), e_y(t, z_j)$ and $e_x(t, z_j)$, respectively. In low S/N environments, it
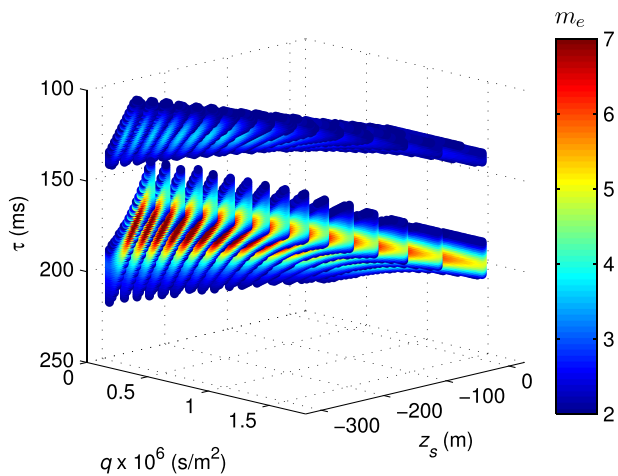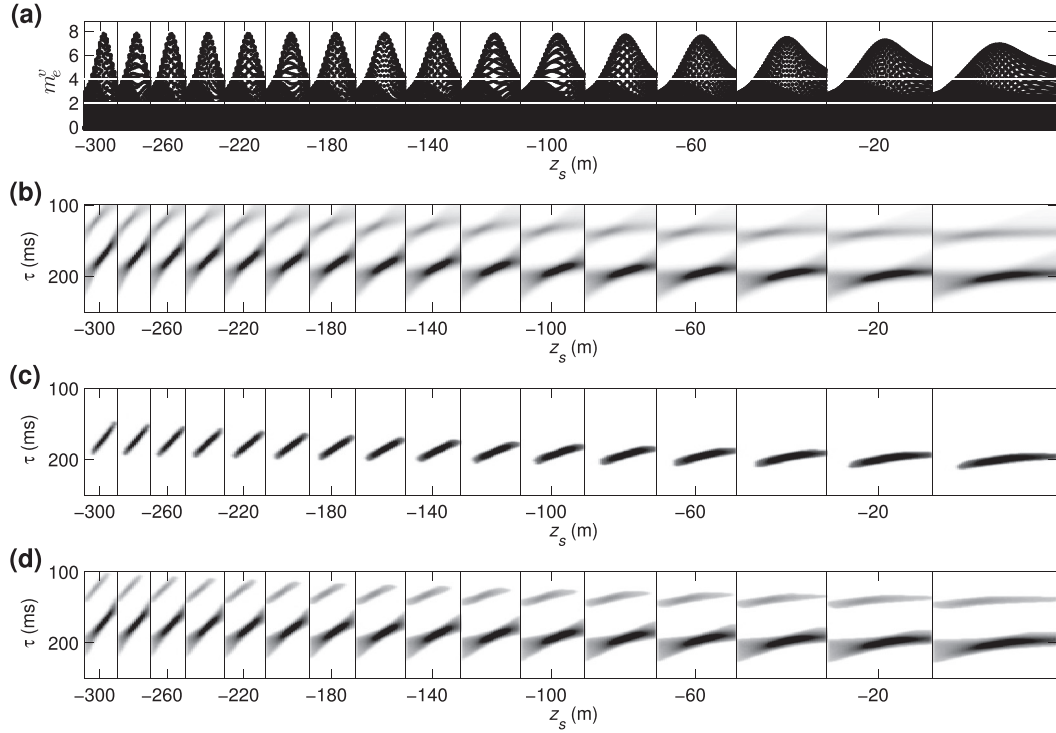

Fig. 2. Synthetic data example 1. Low resolution Radon coefficients $m_e(\tau, q, z_s)$ thresholded using Eq. (7) with $\alpha_1 = 4$. The color-map scale is clipped at 7 so as to make the high amplitudes more clear (recall that the maximum of m_e is 8).

Fig. 3. Synthetic data example 1: Low resolution Radon coefficients of the normalized root mean square envelope. Each panel corresponds to a single source location z_s. (a) Vectorized coefficients m_e^v. The white lines correspond to $\alpha_1 = 4$ and $\alpha_2 = 2$. (b) Radon (τ, q) panels without any thresholding. (c) Radon (τ, q) panels thresholded by $\alpha_1 = 4$ (detection step). (d) Radon (τ, q) panels thresholded by $\alpha_2 = 2$ (denoising step).

is often preferable to detect seismic arrivals by processing the average envelope function of the three-component seismograms (Michaud and Leaney, 2008). In this study, we define the normalized root mean square envelope via the following expression

$$e\left(t, z_j\right) = c_j \sqrt{e_x\left(t, z_j\right)^2 + e_y\left(t, z_j\right)^2 + e_z\left(t, z_j\right)^2}, \quad j = 1, \dots N \tag{5}$$

where the scalar c_j is the normalization factor such that $max[e(t, z_j)] = 1$ for all j. We also define the adjoint apex-shifted parabolic Radon operator over the normalized root mean square envelope via the following sum

$$m_e(\tau, q, z_s) = \sum_z e\left(\tau + q(z - z_s)^2, z\right). \tag{6}$$

This formula can be implemented in an efficient and rapid way by restricting the pairs (q, z_s) after considering the dependency of the minimum and maximum expected arrival times on the parameters q and z_s (Appendix B). By virtue of the normalization of the root mean square envelope, it is clear that an event parameterized by (τ^*, q^*, z_s^*) will lead to $m_e(\tau^*, q^*, z_s^*) \simeq N$. We will use this simple concept to define a criterion in the Radon domain to detect the presence of a microseismic event. In this sense, the presence of an event is detected if there exist parameters (τ^*, q^*, z_s^*) such that

$$m_e\left(\tau^*, q^*, z_s^*\right) \geq \alpha_1, \tag{7}$$

where α_1 is a threshold that can be used to control the sensitivity of the event detection stage. In our code, we adopted $\alpha_1 = N/2$.

2.3. Denoising individual components via a fast ASPRT inversion

Once a microseismic event was identified by the aforementioned detection algorithm criterion, we utilize the ASPRT to denoise individual

components. For this purpose we first use the Radon coefficients obtained from the normalized root mean square envelope to estimate the region of support of the microseismic signal in the space (τ, q, z_s) and to estimate a weighting function that we will utilize to precondition the denoising algorithm.

We first define a matrix of weights via the following expression

$$W_e(\tau, q, z_s) = \begin{cases} m_e(\tau, q, z_s) & \text{if } m_e(\tau, q, z_s) > \alpha_2 \\ 0 & \text{if } m_e(\tau, q, z_s) \leq \alpha_2, \end{cases} \tag{8}$$

where α_2 is another threshold parameter that represents a trade-off between noise rejection and fitting low-amplitude signals. We also define the subset $\mathbb{S}$ of parameters (τ, q, z_s) of identified active coefficients that will be used to fit the data:

$$\mathbb{S} = \{(\tau, q, z_s) \quad \text{such that} \quad m_e(\tau, q, z_s) > \alpha_2\}. \tag{9}$$

Once the support of the signal in Radon space has been found, we propose to use Radon synthesis operator to denoise individual components. In this case we will represent each individual data component as the outcome of the application of the Radon transform to the corresponding series of Radon coefficients. This is expressed mathematically via the following synthesis formula

$$d_c(t, z) = \sum_{(q, z_s) \in \mathbb{S}} m_c\left(t - q(z - z_s)^2, q, z_s\right) \quad \text{for} \quad c = x, y, z. \tag{10}$$

To facilitate the development of the algorithm, the last equation can be written in matrix-vector form using

$$\mathbf{d}_c = \mathbf{L}\mathbf{m}_c + \mathbf{n}_c, \quad c = x, y, z \tag{11}$$

where $\mathbf{d}_c$ corresponds to the c component seismogram, $\mathbf{m}_c$ are the associated Radon coefficients $m_c(\tau, q, z_s)$ in vector form, and $\mathbf{L}$ is the apex-shifted parabolic Radon forward operator. Notice that in Eq. (11) we have also added a noise term. The idea is to estimate the Radon
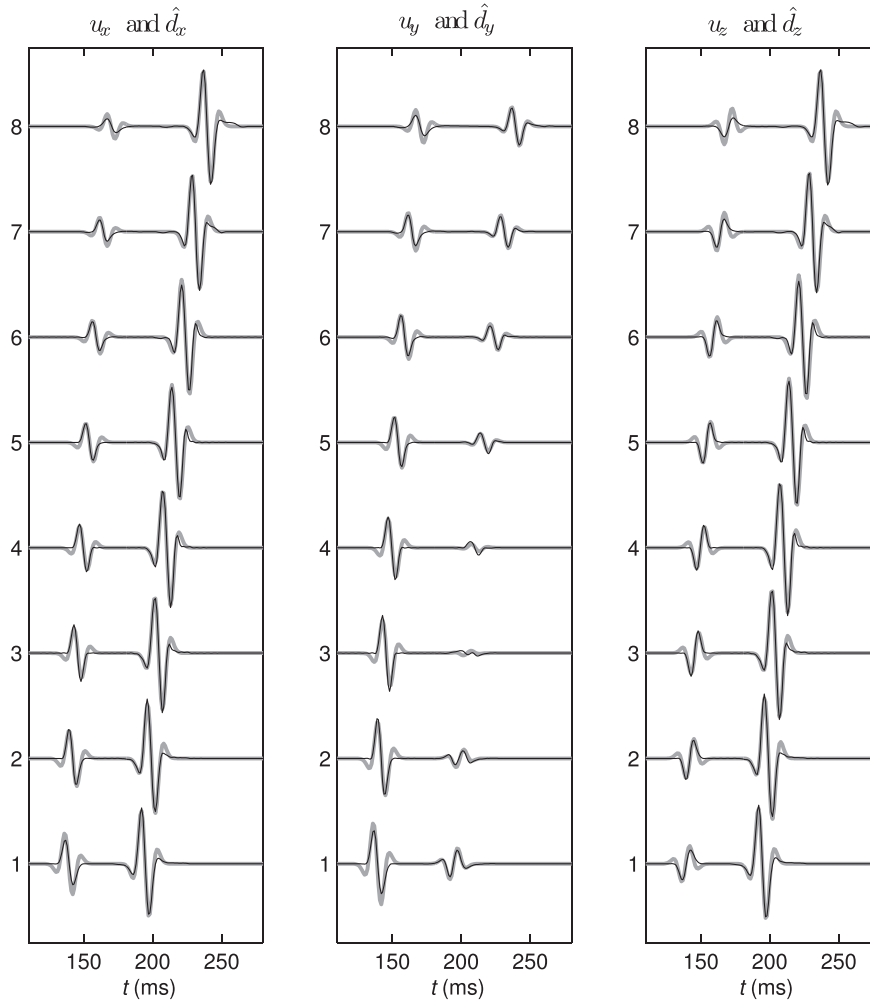
Fig. 4. Synthetic data example 1. The thicker gray lines show the noise-free synthetic data components (u_x, u_y and u_z) and the black lines the corresponding denoised data components ($\hat{d}_x$, $\hat{d}_y$ and $\hat{d}_z$).

coefficients from Eq. (11), and then use the estimated coefficients to synthesize noise-free data. For this purpose, the coefficients are estimated by solving the following problem:

$$\hat{\mathbf{m}}_c = \underset{\mathbf{m}_c}{\operatorname{argmin}} \left[\|\mathbf{L}\mathbf{m}_c - \mathbf{d}_c\|_2^2 + \mu\|\mathbf{P}\mathbf{m}_c\|_2^2 \right], \qquad (12)$$

where $\mathbf{P}$ is a matrix which is applied to the regularization term and μ is a trade-off parameter. We also propose a change of variables $\mathbf{u}_c = \mathbf{P}\mathbf{m}_c$ to rewrite the cost function to minimize in standard form as follows:

$$\hat{\mathbf{u}}_c = \underset{\mathbf{u}}{\operatorname{argmin}} \left[\|\mathbf{L}\mathbf{W}_e\mathbf{u}_c - \mathbf{d}_c\|_2^2 + \mu\|\mathbf{u}_c\|_2^2 \right]$$
$$\hat{\mathbf{m}}_c = \mathbf{W}_e\hat{\mathbf{u}}_c, \qquad (13)$$

where it is clear that we have selected $\mathbf{P}^{-1} = \mathbf{W}_e$ as the preconditioning operator, where $\mathbf{W}_e$ is a diagonal matrix of weights whose elements correspond to $W_e(\tau, q, z_s)$. In essence, we are preconditioning the estimation of the Radon coefficients via a matrix of weights that resembles a semblance function (Moore and Kostov, 2002). The latter is estimated from the average envelope and therefore, it is less prone to be contaminated by the noise in each component. Eq. (13)

is solved using the method of conjugate gradients. Once the solution $\mathbf{m}_c$ is found for an appropriate trade-off value μ, it is used to synthesize an enhanced signal:

$$\hat{\mathbf{d}}_c = \mathbf{L}\hat{\mathbf{m}}_c, \quad c = x, y, z. \qquad (14)$$

This finalizes our denoising stage. We need to stress that the denoising is only carried out when a seismic event is detected. When the detection criterion does not find a seismic event, we simply move to a new window and re-initiate the two-step detection-denoising process.
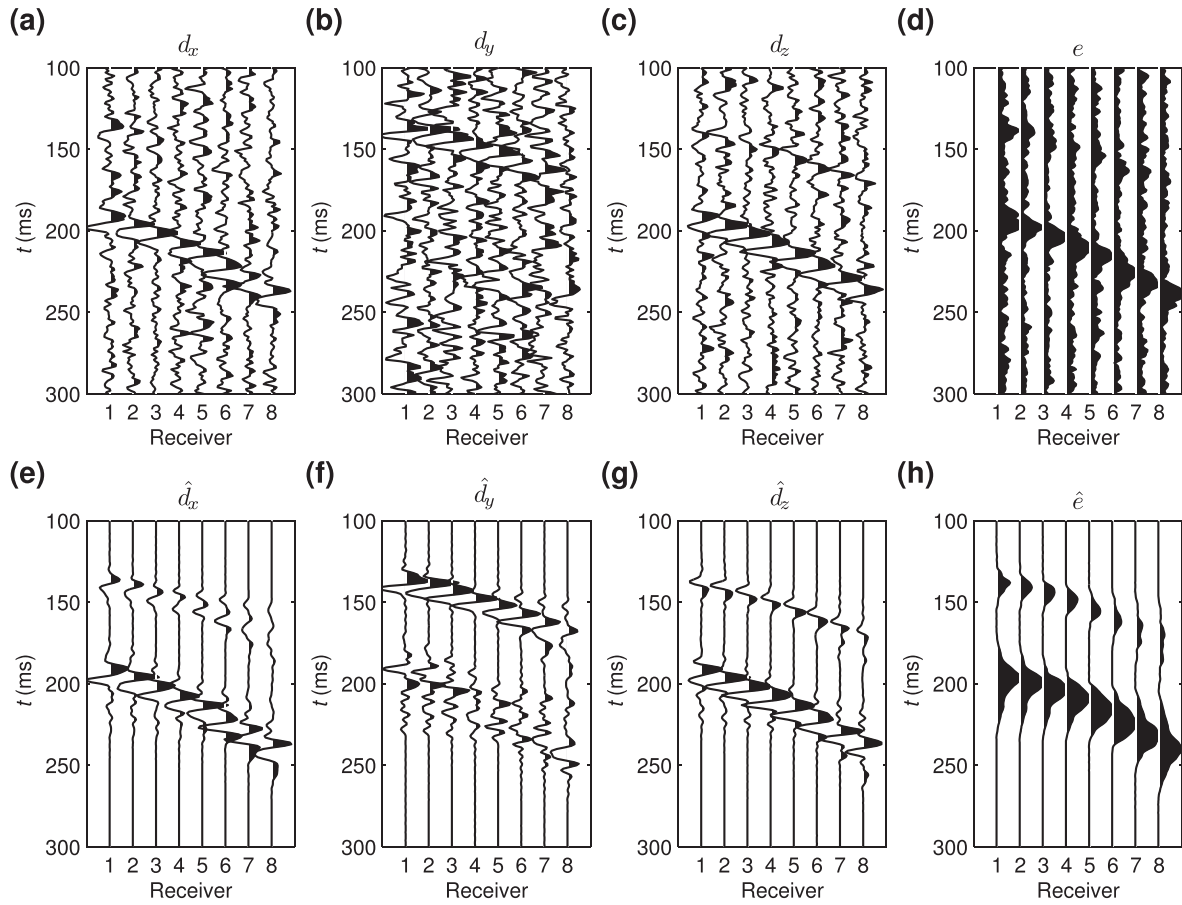
3. Results

We tested our two-step algorithm with synthetic and field data contaminated with different levels of noise.

3.1. Synthetic data

The far-field displacements recorded at each receiver for an homogeneous velocity media are given by Shearer (1999)

$$u_{i(P|S)}(t, \mathbf{x}) = \frac{1}{4\pi\rho c^3} \frac{1}{r} \mathbf{R}_{ijk} \dot{\mathbf{M}}_{jk}\left(t - \frac{r}{c}\right), \qquad (15)$$

Fig. 5. Synthetic data example 2: $S/N = 1.8$. (a) x-component. (b) y-component. (c) z-component. (d) Root mean square envelope attribute e. (e) Denoised x-component. (f) Denoised y-component. (g) Denoised z-component. (h) Denoised root mean square envelope attribute e.
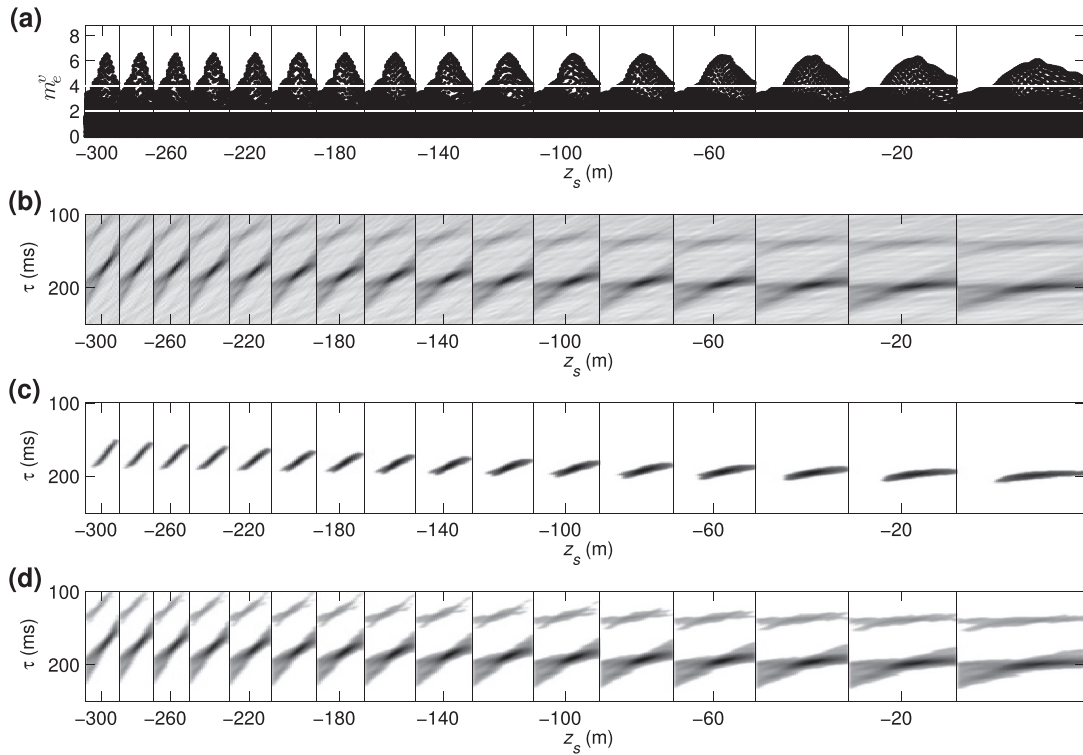
Fig. 6. Synthetic data example 2: Low resolution Radon coefficients of the normalized root mean square envelope. Each panel corresponds to a single source location z_s. (a) Vectorized coefficients m_e^v. The white lines correspond to $\alpha_1 = 4$ and $\alpha_2 = 2$. (b) Radon (τ, q) panels without any thresholding. (c) Radon (τ, q) panels thresholded by $\alpha_1 = 4$ (detection step). (d) Radon (τ, q) panels thresholded by $\alpha_2 = 2$ (denoising step).
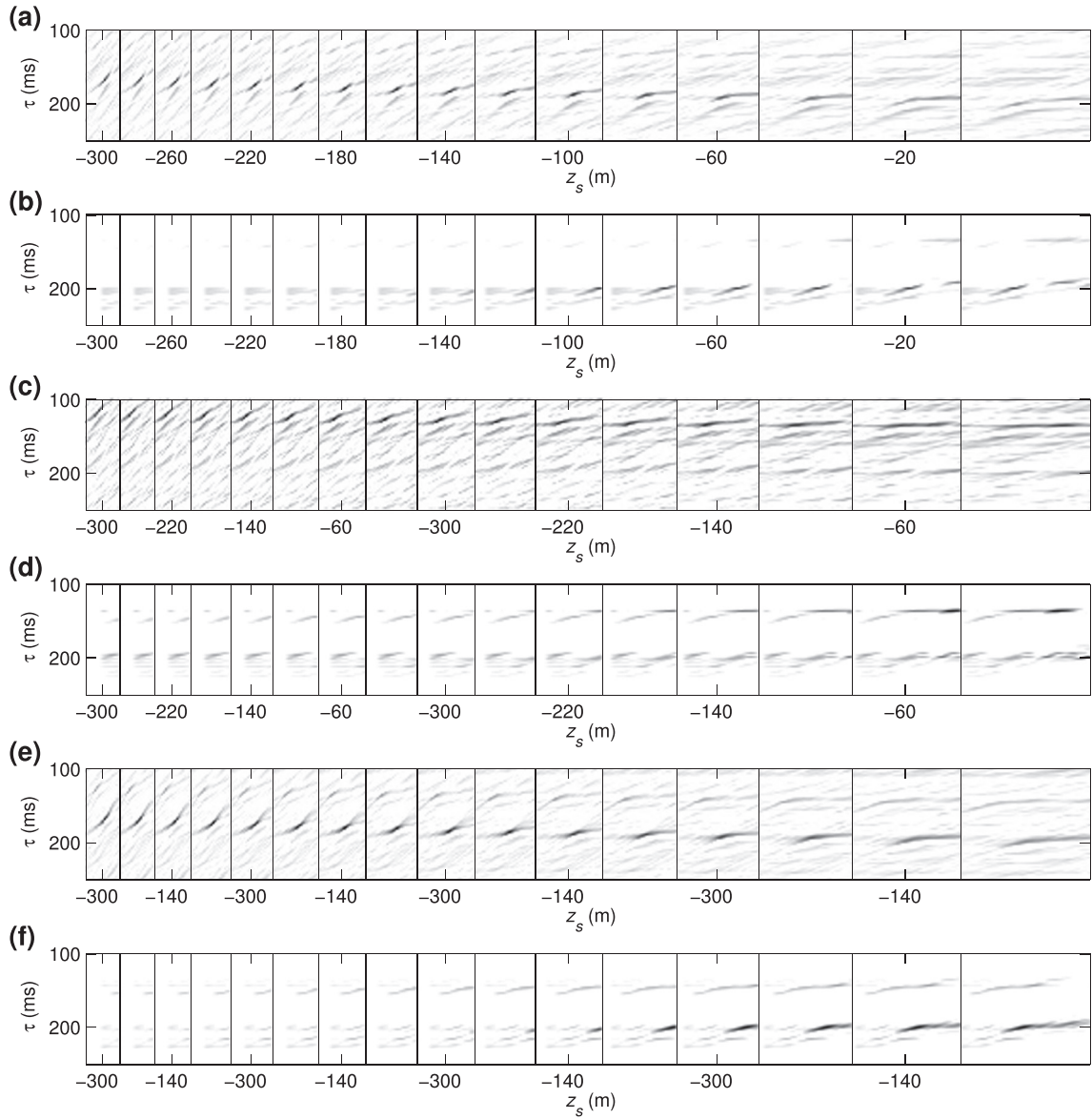
Fig. 7. Synthetic data example 2: Low resolution Radon coefficients for each component and the corresponding Radon coefficients synthesized by the inversion process. (a) Low resolution coefficients for the x-component m_x. (b) Synthesized coefficients for the x-component $\hat{m}_x$. (c) Low resolution coefficients for the y-component m_y. (d) Synthesized coefficients for the y-component $\hat{m}_y$. (e) Low resolution coefficients for the z-component m_z. (f) Synthesized coefficients for the z-component $\hat{m}_z$.

where u_i is the displacement for the component i, $\mathbf{x}$ are the 3D receiver components, ρ is the density of the medium, c is the velocity of the P– or S–wave, r is the distance between the source and the receiver, and $\mathbf{R}_{ijk}$ is the radiation pattern tensor due to the ith receiver component and the jkth element of the seismic moment tensor $\dot{\mathbf{M}}_{jk}$. Assuming that the seismic moment tensor can be separated into a time invariant tensor $\mathbf{M}_{jk}$ and a source time function $s(t)$ (Aki and Richards, 2002):

$$\dot{\mathbf{M}}_{jk} = \mathbf{M}_{jk} s(t). \tag{16}$$
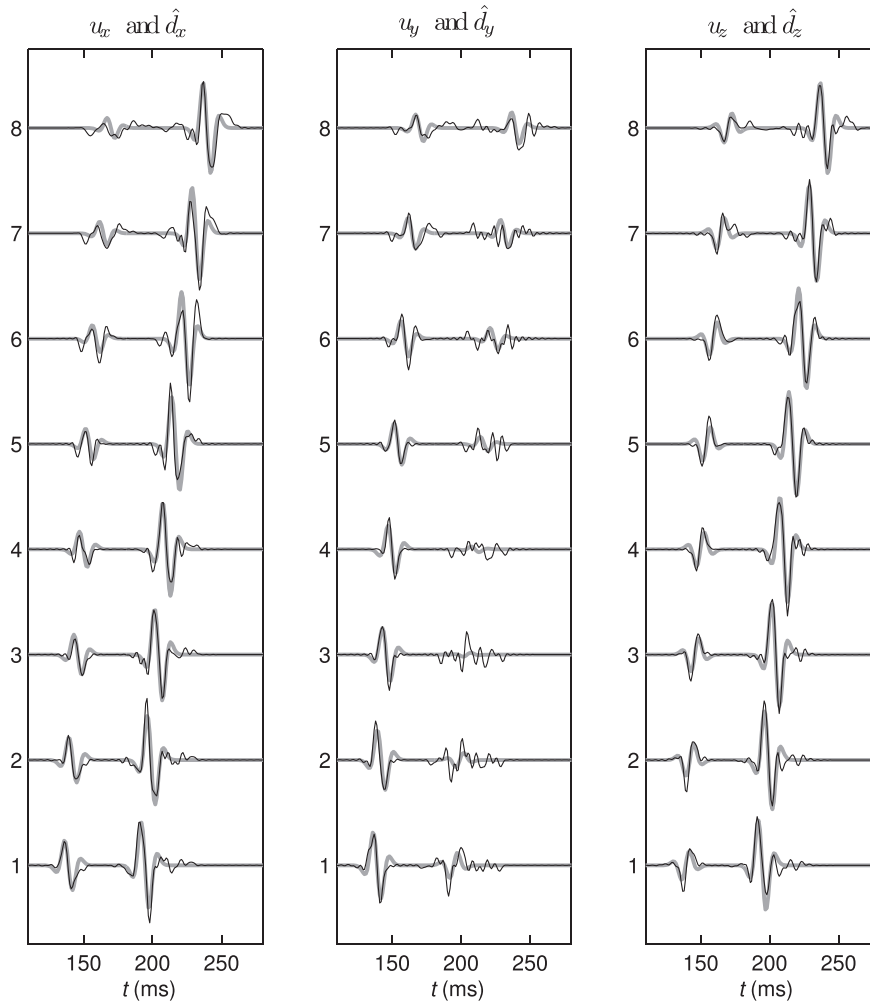
Then, replacing into Eq. (15) yields:

$$u_{i(P|S)}(t, \mathbf{x}) = \frac{1}{4\pi\rho c^3} \frac{1}{r} \mathbf{R}_{ijk} \mathbf{M}_{jk} s\left(t - \frac{r}{c}\right). \tag{17}$$

The synthetic data examples of this work were generated with Eq. (17). We used a medium with $v_P = 3500$ m/s and $v_S = 2400$ m/s.

An array of $N = 8$ multicomponent receivers were vertically located in the medium. For the sake of simplicity, we let the origin of the co-ordinate system be the first (deepest) receiver position. The receivers are thus placed at $\mathbf{x} = (0, 0, \mathbf{z}^r)$, where

$$z_j^r = (j-1)\delta z^r, \quad j = 1, ..., N, \tag{18}$$

with $z_1^r = 0$ m and $\delta z^r = 30$ m. The source was placed at $(x_s, y_s, z_s) = (240, 320, -140)$ m. Note that the horizontal distance h between source and receivers is $h = \sqrt{x_s^2 + y_s^2} = 400$ m. The radiation pattern is a function of the relative position of source and receivers. The source function was modeled via a Ricker wavelet with peak frequency $f_0 = 60$ Hz. To introduce the source mechanism, let us call $\mathbf{k}$ to the unit vector normal to the fault plane and $\mathbf{l}$ to the unit vector of the slip direction. The source was modeled as a shear fracture occurring in the (x, z) plane with the slip in the negative x direction. For that case, $\mathbf{k} = (0, 1, 0)$, $\mathbf{l} = $

$$u_x \quad \text{and} \quad \hat{d}_x \qquad\qquad u_y \quad \text{and} \quad \hat{d}_y \qquad\qquad u_z \quad \text{and} \quad \hat{d}_z$$

Fig. 8. Synthetic data example 2. The thicker gray lines show the noise-free synthetic data components (u_x, u_y and u_z) and the black lines the corresponding denoised data components ($\hat{d}_x$, $\hat{d}_y$ and $\hat{d}_z$).

$(-1, 0, 0)$ and the symmetric moment tensor **M** will be given by Udías (1999):

$$\mathbf{M} = \mathbf{M}_0 \begin{bmatrix} 0 & -1 & 0 \\ -1 & 0 & 0 \\ 0 & 0 & 0 \end{bmatrix}.$$

Finally, we added band-limited random noise to the data.

3.2. Synthetic data example 1

First, we generated a synthetic dataset in a high S/N scenario. This dataset was generated with two purposes: (1) illustrate the proposed technique for the signal detection and denoising, and (2) show that the Radon-based inversion can be used to recover the multicomponent data without degrading the amplitude information that is extremely important for processes like seismic moment tensor inversion (Aki and Richards, 2002; Leaney, 2008). The latter point is not trivial, since Radon transforms assume no amplitude variation effects and microseismic signals are critically affected by amplitude variations caused by the radiation pattern. We will address this point in the section devoted to discussions.

The first data example is shown in Fig. 1 together with the normalized root mean square envelope $e(t, z)$. The S/N was set equal to 100 (negligible noise). Note the radiation pattern effect in the data and particularly the change of polarization of the S–wave in the y-component. To carry out the automatic detection of the microseismic event, we transformed $e(t, z)$ to the Radon domain using the ASPRT. The results are given by the 3D function $m_e(\tau, q, z_s)$, which is illustrated in Fig. 2 using a 3D plot after applying the threshold criterion (Eq. (9)) with $\alpha_2 = 2$. The amplitude of each $m_e(\tau, q, z_s)$ value is shown with a color-map scale. Fig. 2 shows that each value of the scanned source depth z_s gives rise to a different Radon panel in the (τ, q) domain. One can easily identify the P– and the S–wave energy. Notice that there is a large subset of parabolas stacking over the same microseismic event, especially for the S–wave.

Another way of visualizing and analyzing the Radon coefficients amplitudes is by re-organizing $m_e(\tau, q, z_s)$ into a 1D array m_e^v. This "vectorized" new array is shown in Fig. 3a to illustrate the detection and denoising threshold criteria. Each panel corresponds to a scanned source depth z_s. Each dot corresponds to a pair (τ, q). As we limited the number of parabolas, the number of q values for each z_s is not constant. Therefore, each panel has a different size. The white lines at $m_e^v = 4$ and $m_e^v = 2$ correspond to $\alpha_1 = 4$ and $\alpha_2 = 2$ for the detection and denoising thresholds, respectively. We additionally computed a 2D
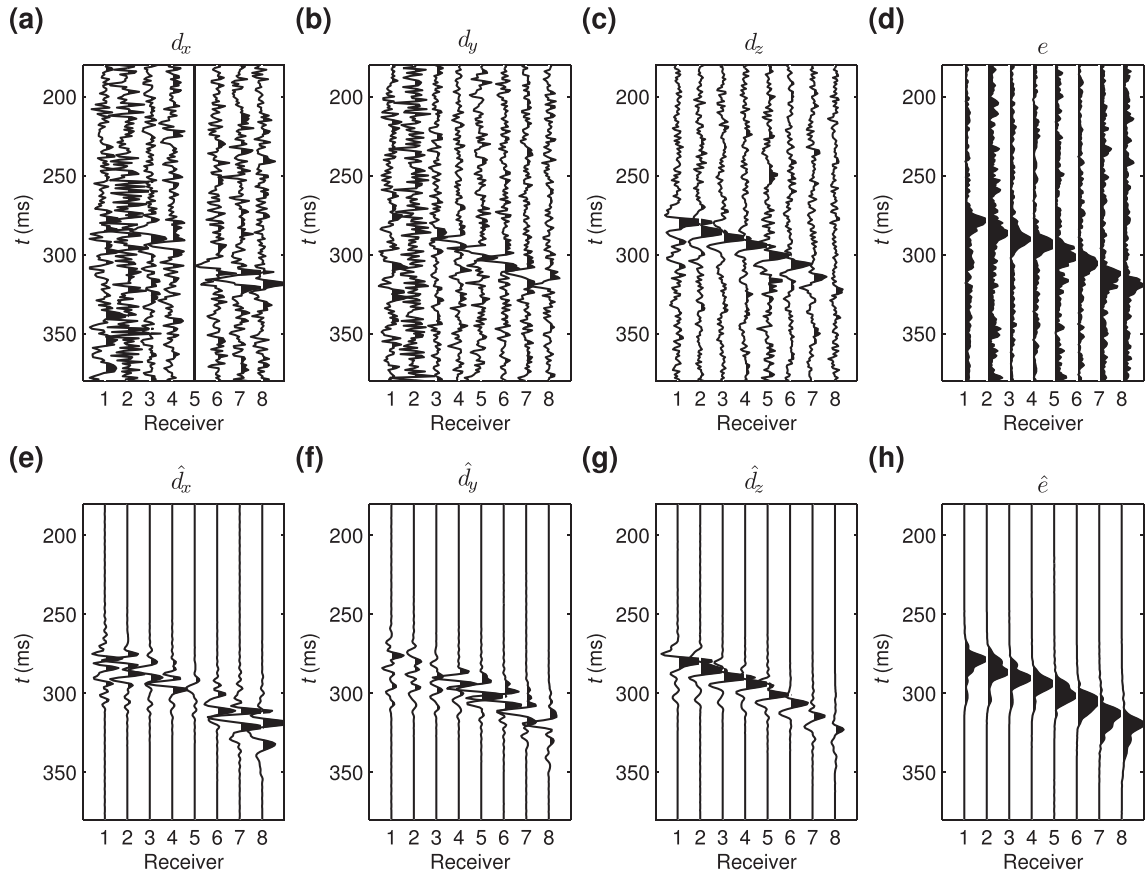
Fig. 9. Field data example 1 (high *S/N* case): (a) *x*-component. (b) *y*-component. (c) *z*-component. (d) Root mean square envelope attribute *e*. (e) Denoised *x*-component. (f) Denoised *y*-component. (g) Denoised *z*-component. (h) Denoised root mean square envelope attribute *e*.

Radon panel $m_e(\tau, q)$ for every source position z_s. These panels are shown in Fig. 3b with no threshold, in Fig. 3c thresholded by $\alpha_1 = 4$, and in Fig. 3d thresholded by $\alpha_2 = 2$. Fig. 3 demonstrates that the signal detection, in this case, is due to the S–wave arrival energy, because the P–wave energy is below α_1 but above α_2. By comparing Fig. 3b with Fig. 3d one can notice that a small portion of low amplitude signal will not be considered in the subset $\mathbb{S}$ used for the denoising step.

Once the event was detected via the α_1-thresholding, we synthesized the Radon representation for each data component with Eq. (13) using the subset $\mathbb{S}$ that is derived after applying the α_2-thresholding (Fig. 3d). The denoised components are obtained transforming back to the time domain with the forward operator (Eq. (14)). The results are shown in Fig. 4 (black lines) superimposed onto the synthetic noise-free data components (gray lines). In this example, denoising was not problematic because $S/N = 100$. However, we stress that the waveform and amplitudes were recovered with great accuracy, especially for the S–wave. Note that in the *y*-component of the S–wave the arrivals present a change of polarity and the signal amplitudes are very low due to the radiation pattern. Nonetheless, we observe a remarkable agreement between the observed and predicted data. The only significant discrepancies that arise are observed for the P–wave, where some low amplitude side-lobes were missed. These discrepancies can be explained as follows: these arrivals exhibit low amplitude and thus the number of Radon coefficients that passed the α_2-thresholding is very small.

3.3. Synthetic data example 2

The second synthetic example was generated using $S/N = 1.8$. The data components, the normalized root mean square envelope, and the

denoised data are shown in Fig. 5. The P–wave signal was masked by the noise in the *x*- and *z*-components. The noise also corrupted the *y*–component of the S–wave. The P–wave arrivals are hardly distinguishable by visual inspection, not even analyzing the normalized root mean square envelope (Fig. 5d). However, the method succeeded in cleaning the microseismic arrivals for both the P– and the S–wave signals.

In Fig. 6 we show the vectorized 1D array m_e^v Radon coefficients and the Radon (τ, q) panels that lead to our detection criterion and to the domain restriction we used for the denoising. By comparing Fig. 6b and d it is clear that the α_2-thresholding rejected most of the noise components. In Fig. 7 we show the low resolution Radon panels for each data component and the synthesized coefficients that result from the inversion. The low resolution coefficients (Fig. 7a, c and e) were estimated using the adjoint operator (Eq. (6)) without the thresholding. It is interesting to note that the S–wave microseismic arrival energy is clear in the *x*- and *z*-components (see Fig. 7a and e, respectively), while the P–wave microseismic arrival energy is clear in the *y*-component only (Fig. 7c). However, in our automatic strategy, we do not have this information in advance. We are only exploiting the information given by $m_e(\tau, q, z_s)$ to synthesize each data component. For this reason, in Fig. 7b, d and e the signal is highly focused on the coefficients shown in Fig. 6d.

Finally, to evaluate the denoising results, we present the noise-free data together with the denoised traces in Fig. 8. The amplitudes and waveforms were very well recovered, except for those components and phases for which the signal was totally masked by the noise. Particularly, the S–wave signal amplitude is very low in the *y*-component, and the algorithm outputs noise in these cases.
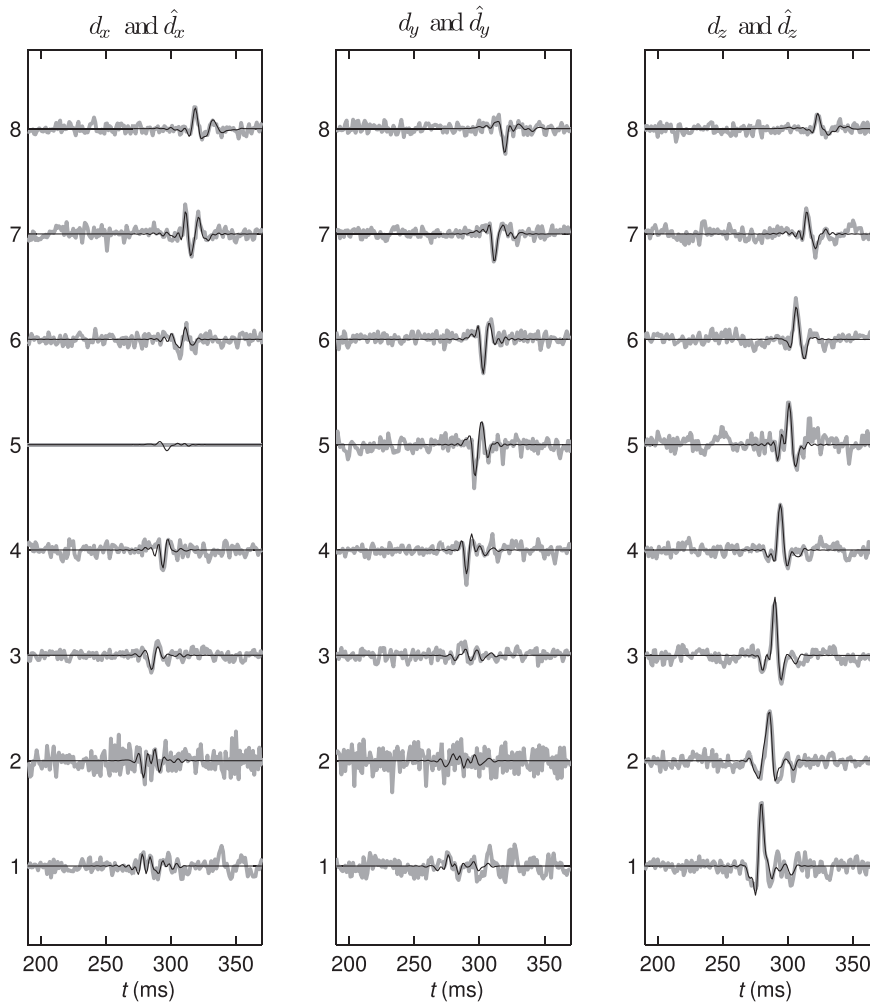
Fig. 10. Field data example 1 (good S/N case). The thicker gray lines show the raw data components (u_x, u_y and u_z) and the black lines the corresponding denoised data components ($\hat{d}_x$, $\hat{d}_y$ and $\hat{d}_z$).

3.4. Field data example 1

We tested the algorithm with field datasets with different S/N. The first dataset is shown in Fig. 9 (top row). Only a single phase arrival is above the noise level. Assuming that the source mechanism is a shear fracture, this energy is probably due to the S–wave. The 5th channel of the x-component is corrupted and so we muted it. Although the records are noisy, the event was very well isolated by the algorithm (see Fig. 9e, f and g). Nonetheless, one should note that although the signal is severely contaminated by the noise in the x- and y-components, the S/N of the z-component is relatively high. This makes the proposed detection-denoising strategy perform very well.

We show a detailed view of the results in Fig. 10, where we superimposed the raw traces onto the corresponding denoised ones. We point out that the original noise-free data are not available for these field data examples. Nevertheless, one can evaluate the results after noting that the algorithm performed as expected by recovering consistent waveforms at the appropriate locations in most of the individual traces. However, it is very difficult to assess, for example, whether in channels 1 and 2 for the x- and y-components (where the S/N is very low) the algorithm outputs noise or the actual signal. Likewise, we intentionally let the method invert the muted trace (5th channel of the x-component). As a result, a low amplitude signal consistent with the nearby waveforms was "reconstructed" after the process.
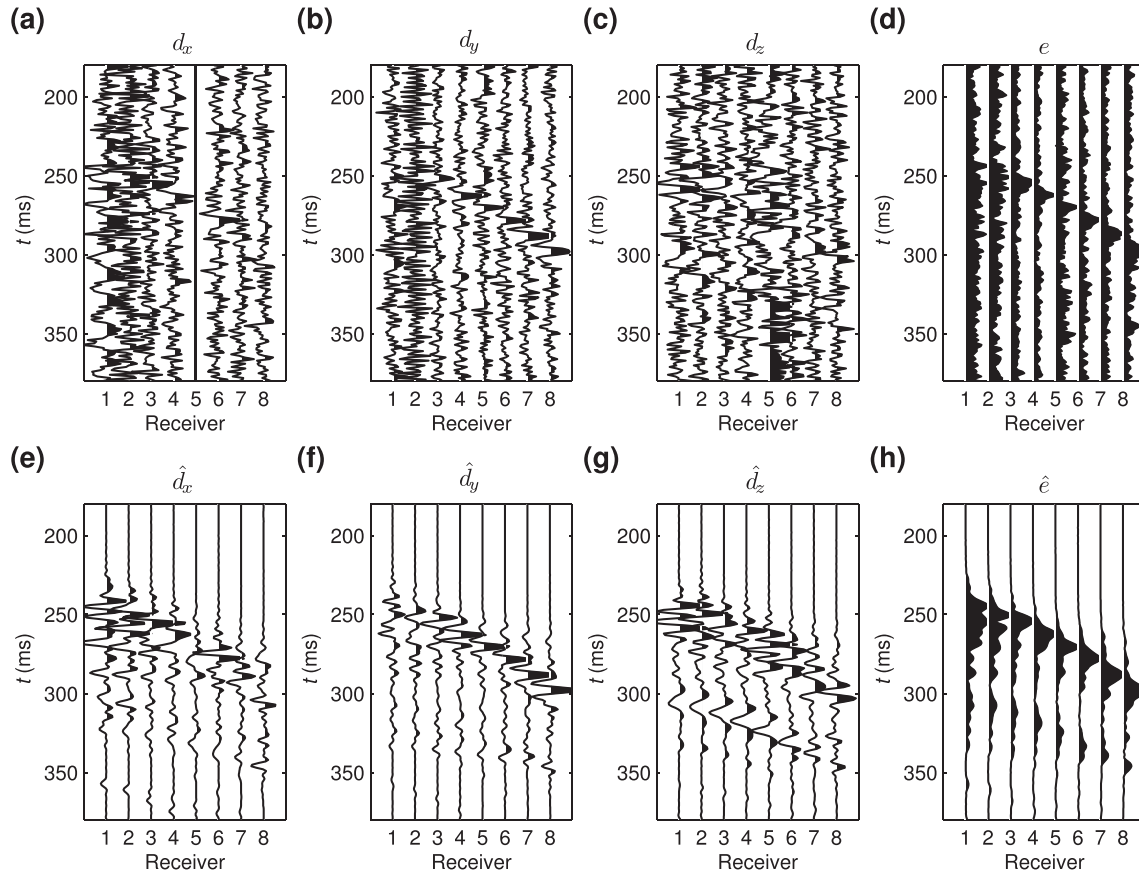
3.5. Field data example 2

The second field dataset is shown in Fig. 11 (top row). This dataset is more challenging than the previous one, because most traces are very noisy. Despite the fact that the microseismic arrivals are only easily distinguishable in the y-component, the use of the normalized root mean square envelope e helps to increase the confidence of the signal detection. We show the results of the event detection and denoising in Fig. 11 (bottom row). Although the results are not optimal, we want to stress that the detection is obtained automatically. Further, the S/N is increased significantly after the denoising step, even for those channels where the signal arrival was barely distinguishable.

Fig. 12 compares the individual raw traces with the denoised ones. Again, the algorithm succeeded to denoise those traces in which the microseismic arrivals are not completely masked by the noise (particularly for the y-component). On the other hand, and due to the extremely low S/N, the signal cannot be isolated in some channels. Nevertheless, the denoised data provide an acceptable solution of improved quality as compared with the original data.

4. Discussion

There are some hypothesis and assumptions made by our algorithm that are worth discussing. First, our method is derived using the constant velocity assumption. However, the velocity we are considering

Fig. 11. Field data example 2 (low S/N case): (a) x-component. (b) y-component. (c) z-component. (d) Root mean square envelope attribute e. (e) Denoised x-component. (f) Denoised y-component. (g) Denoised y-component. (h) Denoised root mean square envelope attribute e.

has not a strict physical meaning. In Eqs. (1) and (2), for example, one should interpret the parameter v as an "effective" velocity (Yilmaz, 2001; Blias and Grechka, 2013). Moreover, after the parabolic approximation, we are just considering those triplets (τ, q, z_s) that best stack over the microseismic signal. Therefore, v is a parameter related to τ and q (see Eqs. (3) and (4)) which does not need to have a physical meaning.

The second hypothesis of the proposed algorithm is related to the parabolic approximation. We showed in Appendix A that for some geometries this should not be a problem, in spite of the errors that may arise by considering a parabola instead of an hyperbola in cases with large array apertures. For those scenarios, an alternative solution is to consider the actual hyperbolic arrivals times and use an apex-shifted hyperbolic Radon transform (Sabbione et al., 2013). However, a hyperbolic Radon transform is a 4D mapping that involves the scanning of an extra parameter for a 2D geometry model. Although more accurate, the computational cost increases significantly with respect to the proposed ASPRT, and fast almost real-time processing could not be considered. In other words, the parabolic Radon-based algorithm proposed in this work can be used to detect microseismic signals in real time, while the hyperbolic Radon-based method cannot.

The third and last hypothesis assumed in this work has to do with the representation of the data in the Radon domain. We could, for instance, have adopted the high resolution Radon transform (Thorson and Claerbout, 1985; Sacchi and Ulrych, 1995; Trad et al., 2003) that assumes that parabolic events can be modeled via a small number of coefficients in the Radon panel. This is true when seismic reflections exhibit a moderate amplitude variation with offset (AVO) effect. A high resolution Radon transform that preserves AVO effects has been proposed by Wang et al. (2011). However, this algorithm requires the estimation of two Radon panels: one to model the intercept and one to model the

gradient. Modeling radiation patterns is more difficult than modeling moderate AVO effects. In addition, AVO preserving Radon algorithms are more expensive in terms of computational cost than traditional algorithms. The latter is the main reason why we have not utilized AVO preserving high resolution Radon transform algorithms to model microseismic data. We do understand that the forward Radon operator that we have proposed in this paper cannot handle strong variations of amplitudes caused by radiation patterns if one were to invert it via a sparsity constraint. This is why we resorted to utilize a least-squares Radon transform with pre-defined regions of support and with a preconditioning operator derived from the average envelope. Given that the Radon transform panel is non-sparse and contains many coefficients in the area of support of the elements (τ, q, z_s), the strong radiation patterns are modeled without incurring the problems associated with the mismatch that exists between observed and modeled responses. Nevertheless, a few low-amplitude discrepancies may arise as we showed in the first synthetic data example.

Our method requires two parameters: the threshold α_1 for the automatic signal detection and the threshold α_2 for the Radon domain restriction that leads to the S/N enhancement. The detection criterion is simple and relies in a single parameter easily tuned by virtue of the normalization of the root mean square envelope. In fact, we set $\alpha_1 = N/2$ in all examples, where N is the number of receivers. The algorithm was devised to be applied in partially-overlapped moving windows that scan for microseismic events automatically. In this work we only show windows containing a single microseism after the event detection step. However, the method permits to denoise more than one event within the window of analysis. This situation is equivalent to detecting two phases (as shown in the synthetic examples) where the S–wave masks the P–wave and the algorithm denoised the signal correctly. We should stress that although we did not show the complete datasets,
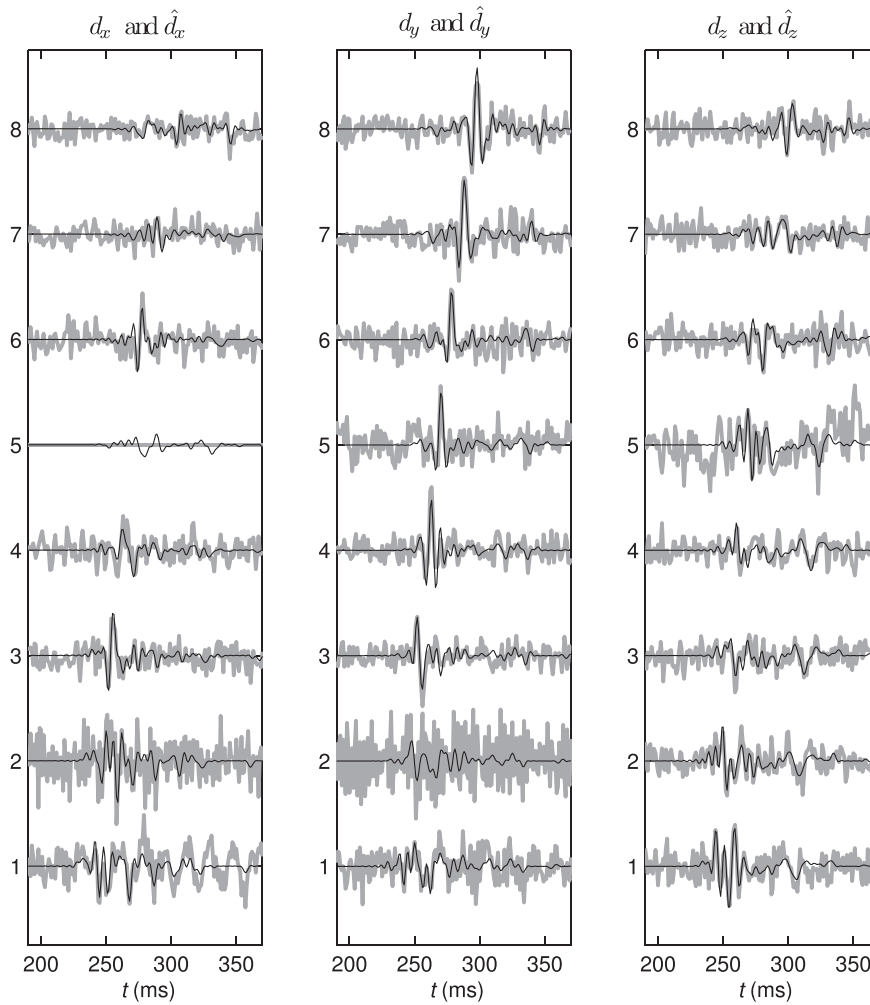
Fig. 12. Field data example 2 (poor S/N). The thicker gray lines show the raw data components (u_x, u_y and u_z) and the black lines the corresponding denoised data components ($\hat{d}_x$, $\hat{d}_y$ and $\hat{d}_z$).

there were no false detections neither for the synthetic nor for the field data examples. In this sense, the largest Radon coefficient $max[m_e]$ within the analyzed window acts as a confidence indicator. The likelihood of detecting a false event is high when $max[m_e]$ is close to α_1. In practice, we use $max[m_e]$ to asses the reliability of the corresponding detected event. Regarding the domain restriction, the selection of α_2 is a trade-off between preserving low-amplitude signals and noise rejection. In other words, α_2 could be related to the S/N of the microseismic data. We believe that in general $\alpha_2 = N/4$ is a good figure to reject most of the noise energy and to avoid killing the signal.

Although surface monitoring arrays are beyond the scope of this work, we briefly discuss how one could generalize the proposed method to cope with surface microseismic data (Thornton and Eisner, 2011). In this situation, we need to consider a 3D scenario to model the data. Assuming that the parabolic approximation is valid for surface geometries, it can be shown that traveltimes are aligned along an apex-shifted paraboloid in the (x, y) domain. Therefore, the computational cost of the method increases significantly because two extra parameters are required in the summations.

5. Conclusions

We presented an algorithm that tackles two of the main problems in microseismic downhole data processing: (1) automatic signal detection and (2) data denoising. The methodology is based on an apex-shifted parabolic Radon transform. The algorithm was derived using the constant velocity model but it is clear that parabolic approximations can

also be used in situations where the velocity model is not constant. The parabolic parameter q is a simple curvature parameter and should not be used to estimate velocity information.

The algorithm can be divided into two steps. In the first step, the microseismic arrivals are automatically detected based on the low resolution Radon coefficients of the normalized root mean square envelope of the 3C data. The second step is devised to denoise the data via an adaptive filtering technique. Once an event was detected, the information given by the aforementioned Radon coefficients is exploited in two different ways. First, to restrict the Radon domain and focus on the microseismic signal energies. Secondly, to precondition the Radon synthesis of each data component. The representation of the data components for the denoising step is posed as an inverse problem and solved by the conjugate gradients method. The synthesized Radon coefficients for each data component are used to transform back to the data domain thus obtaining a denoised version of the input data.

The computational cost of the Radon transforms is critically reduced by restricting the number of parabolas that are expected to arise based on moveout considerations, and also by the Radon domain restriction for the denoising step. Therefore, the method is computational efficient and could be used to process microseismic data in real time.

The results using synthetic data examples show that the detection is triggered by the phase with higher energy (the S–wave in our examples). In addition, the proposed strategy inverts the microseismic signal waveforms properly despite of the difficulties that entail the complicated radiation pattern. The discrepancies on the amplitudes are not

considerable, nonetheless some low-amplitude side-lobes can be missed. The test over a noisy synthetic dataset demonstrates that the algorithm significantly enhanced the S/N of the input data for both the P– and the S–wave arrivals. Regarding the field data examples, the method succeeded in detecting the arrivals automatically for both the good and the poor S/N cases. The denoised version of the good S/N dataset exhibits signal arrivals which are very well isolated and cleaned. For the example with poor S/N, those traces with visually distinguishable arrivals were properly denoised. However, for seismograms with poor S/N, the inversion tends to retain the noise. Synthetic data tests show that one should rely on these denoised traces. In any case, for very noisy data, an expert analyst can simply isolate the part of the signal were the microseismic was detected.

We believe that this method represents a very useful tool to be applied in standard downhole microseismic data processing. In general, the method is very robust to detect the events automatically, and contributes to significantly enhance the data quality for further data processing.

Acknowledgments

Appendix A. The validity of the parabolic approximation

In this appendix we demonstrate the validity of the parabolic Radon transform approximation in the context of microseismic event detection and denoising. In addition, we show the discrepancies that can arise when adopting this approximation instead of the expected hyperbolic model. In this sense, the parabola that best approximates the true hyperbolic travel time is also the parabola that maximizes the energy of the parabolic Radon transform. Therefore, parameters (τ, q) represent the "effective" intercept and curvature coefficients that best approximate a waveform with hyperbolic travel-time. To begin with, consider the following approximation:

$$\tau + q(z-z_s)^2 \approx t_0 + \sqrt{\frac{(x-x_s)^2}{v^2} + \frac{(z-z_s)^2}{v^2}}. \tag{A.1}$$

For an N-receivers vertical array with coordinates $(x, z_j), j = 1, ..., N$, we can write Eq. (A.1) in matrix notation

$$A\zeta = Y, \tag{A.2}$$

where

$$A = \begin{bmatrix} 1 & (z_1-z_s)^2 \\ 1 & (z_2-z_s)^2 \\ \vdots & \vdots \\ 1 & (z_N-z_s)^2 \end{bmatrix}, \zeta = \begin{bmatrix} \tau \\ q \end{bmatrix}, Y = \begin{bmatrix} t_0 + \sqrt{\frac{(x-x_s)^2}{v^2} + \frac{(z_1-z_s)^2}{v^2}} \\ t_0 + \sqrt{\frac{(x-x_s)^2}{v^2} + \frac{(z_2-z_s)^2}{v^2}} \\ \vdots \\ t_0 + \sqrt{\frac{(x-x_s)^2}{v^2} + \frac{(z_N-z_s)^2}{v^2}} \end{bmatrix}$$

The parameters (τ, q) that best satisfy Eq. (A.2) according to the least-squares criterion are given by:

$$\zeta = \left(A^\top A\right)^{-1} A^\top Y. \tag{A.3}$$

In Fig. A.13a we show a typical geometry for this problem. The velocity model is constant with $v = 2500$ m/s. The dots represent potential source locations. Their sizes are proportional to the rms error between the hyperbolic travel-times and the parabolic travel-times computed using the effective parameters derived from Eq. (A.3). It is clear that the error increases as the source moves away from the receiver array in the vertical coordinate, and/or approaches the receiver array in the horizontal coordinate. Nonetheless, the errors are relatively small, as shown in Fig. A.13b. To further analyze the validity of the approximation, we selected two sources: one in the center of the analyzed positions, and the other in the worst situation regarding the errors generated by the approximation. The selected sources and their corresponding rms errors are indicated in Fig. A.13a and b, respectively. The actual hyperbolic travel-times and those obtained by the parabolic approximations after solving Eq. (A.3) are shown in Fig. A.13c. Notice that the approximation is suitable for these geometries, for one can find a pair (τ, q) that fits the curve very accurately. Therefore, the small discrepancies observed in Fig. A.13c should not represent a major concern given the implicit errors introduced by the constant velocity assumption. Nevertheless, it is worth mentioning that receiver arrays with larger apertures will produce larger errors. In such cases, one should perform an rms-analysis similar to the one carried out in this appendix in order to validate the hyperbolic assumption before applying the detection/denoising algorithm.

Appendix B. Restriction of parabolic paths to increase the computational efficiency of the method

We are approximating the hyperbolic arrivals given by Eq. (1) by the parabolas given by Eq. (3). The computational cost of the Radon transform is mainly determined by the sums in Eq. (6). Microseismic arrivals are not expected to be horizontally aligned along the records.
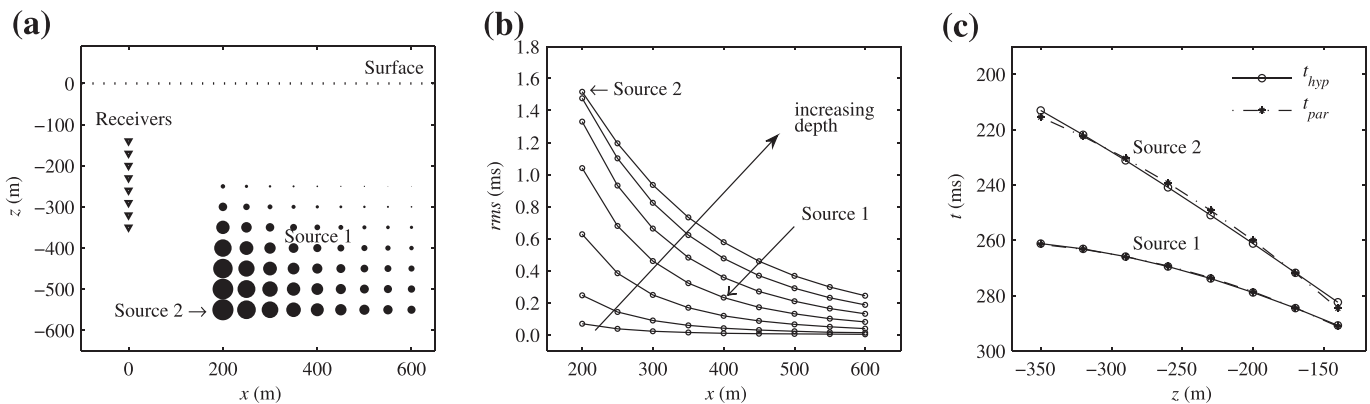
Fig. A.13. Parabolic approximation analysis. (a) Typical geometry in downhole acquisition projects. The black dots represent possible source locations. The size of the dot is proportional to the rms error between the actual and the approximated travel-times. (b) rms error curves for the different source depths in (a). (c) Hyperbolic arrival times and their corresponding times for the parabolic approximation for the two selected sources.
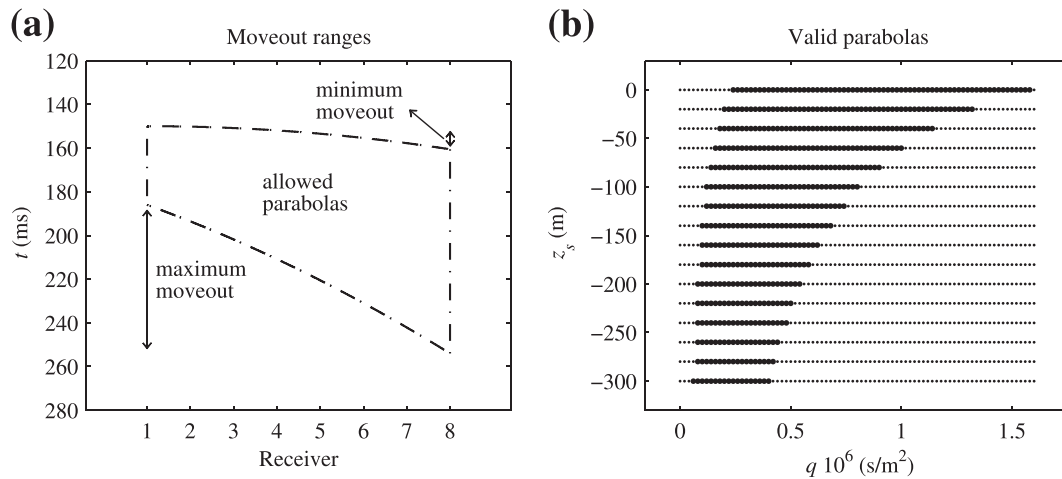
Fig. B.14. (a) Region for the allowed parabolas defined by the minimum and maximum moveouts. (b) Valid parabolas for the Radon operators. The bigger dots depict the valid (τ, q) pairs. The smaller dots depict the (τ, q) pairs that are rejected and not considered in the Radon transform operators.

In addition, the maximum moveout between any pair of receivers should also be bounded. We use this idea to restrict the number of (q, z_s) pairs involved in the Radon operators. Given the known receivers locations, we fix the minimum and maximum expected moveouts for the signal arrivals. Using Eq. (3), this limit values define a region in the (t, z) record domain, as shown in Fig. B.14a. Each pair (q, z_s) that generates a parabola outside this region is not taken into account for the Radon operators. By these means, we significantly reduce the number of calculations and increase the efficiency of the algorithm (see Fig. B.14b). Moreover, the parabolas restriction also contributes to diminish the risk of stacking over false events.

References

Aki, K., Richards, P.G., 2002. Quantitative Seismology. 2nd edition. University Science Books.

Blias, E., Grechka, V., 2013. Analytic solutions to the joint estimation of microseismic event locations and effective velocity model. Geophysics 78 (3), KS51–KS61.

Eisner, L., Duncan, P.M., Heigl, W.M., Keller, W.R., 2009. Uncertainties in passive seismic monitoring. Lead. Edge 28 (6), 648–655.

Eisner, L., Thornton, M., Griffin, J., 2011. Challenges for microseismic monitoring. SEG Expanded Abstractspp. 1519–1523.

Forghani-Arani, F., Willis, M., Haines, S., Batzle, M., Behura, J., Davidson, M., 2013. An effective noise-suppression technique for surface microseismic data. Geophysics 78 (6), KS85–KS95.

Hampson, D., 1986. Inverse velocity stacking for multiple elimination. J. Can. Soc. Explor. Geophys. 22 (1), 44–55.

Hargreaves, N., verWest, B., Wombell, R., Trad, D., 2003. Multiple attenuation using an apex-shifted Radon transform. SEG Expanded Abstracts 22 (1) pp. 1929–1932.

Kendall, M., Maxwell, S., Foulger, G., Eisner, L., Lawrence, Z., 2011. Special section. Microseismicity: beyond dots in a box — introduction. Geophysics 76 (6), WC1–WC3.

Leaney, W.S., 2008. Inversion of microseismic data by least-squares time reversal and waveform fitting. SEG Expanded Abstractspp. 1347–1351.

Maxwell, S.C., Urbancic, T.I., 2001. The role of passive microseismic monitoring in the instrumented oil field. Lead. Edge 20 (6), 636–639.

Maxwell, S.C., Rutledge, J., Jones, R., Fehler, M., 2010. Petroleum reservoir characterization using downhole microseismic monitoring. Geophysics 75 (5) (75A129-75A137).

Michaud, G., Leaney, S., 2008. Continuous microseismic mapping for real-time event detection and location. SEG Expanded Abstracts 27 (1) pp. 1357–1361.

Moore, I., Kostov, C., 2002. Stable, efficient, high-resolution Radon transforms. EAGE, Extended Abstracts p. F-34.

Russell, B., Hampson, D., Chun, J., 1990a. Noise elimination and the Radon transform, part 1. Lead. Edge 9 (10), 18–23.

Russell, B., Hampson, D., Chun, J., 1990b. Noise elimination and the Radon transform, part 2. Lead. Edge 9 (11), 31–37.

Sabbione, J.I., Velis, D.R., Sacchi, M.D., 2013. Microseismic data denoising via an apex-shifted hyperbolic Radon transform. SEG Expanded Abstracts pp. 2155–2161.

Sacchi, M.D., Ulrych, T.J., 1995. High-resolution velocity gathers and offset space reconstruction. Geophysics 60 (4), 1169–1177.

Shearer, P.M., 1999. Introduction to Seismology. Cambridge University Press.

Thornton, M., Eisner, L., 2011. Uncertainty in surface microseismic monitoring. SEG Expanded Abstractspp. 1524–1528.

Thorson, J.R., Claerbout, J.F., 1985. Velocity-stack and slant-stack stochastic inversion. Geophysics 50 (12), 2727–2741.

Trad, D., 2003. Interpolation and multiple attenuation with migration operators. Geophysics 68 (6), 2043–2054.

Trad, D., Ulrych, T., Sacchi, M., 2003. Latest views of the sparse radon transform. Geophysics 68 (1), 386–399.

Udías, A., 1999. Principles of Seismology. Cambridge University Press.

Vera Rodriguez, I., Bonar, D., Sacchi, M., 2012. Microseismic data denoising using a 3C group sparsity constrained time-frequency transform. Geophysics 77 (2), V21–V29.

Wang, B., Sacchi, M.D., Jin, X.Y., 2011. AVO-preserving sparse parabolic Radon transform. 73rd EAGE Conference & Exhibition.

Yilmaz, O., 1989. Velocity-stack processing. Geophys. Prospect. 37, 357–383.

Yilmaz, O., 2001. Seismic data analysis: processing, inversion, and interpretation of seismic data. Investigations in Geophysics. SEG.